coatings

MDPI

Article

Enhancement of Ferroelectric Properties of Ni-Substituted $Pb_2Fe_2O_5$ Thin Films Synthesized by Reactive Magnetron Sputtering Deposition

Benas Beklešovas, Vytautas Stankus, Aleksandras Iljinas * and Ugnė Balčiūnaitė

Department of Physics, Kaunas University of Technology, Studentu Str. 50, LT-51368 Kaunas, Lithuania; benas.beklesovas@ktu.lt (B.B.); vytautas.stankus@ktu.lt (V.S.); ugne.balciunaite@ktu.edu (U.B.)
* Correspondence: aleksandras.iljinas@ktu.lt

Abstract: Lead ferrite $Pb_2Fe_2O_5$ (PFO) is a potential multiferroic material due its exhibition of ferroelectric and ferromagnetic properties. The effects of the substitution with nickel and synthesis temperature on the structural, morphological, and ferroelectric properties of lead ferrite thin films were investigated through the use of reactive magnetron sputtering deposition. Nickel loading concentrations were systematically varied (3%, 5%, and 10% by wt.%). X-ray diffraction analysis confirmed the formation of Ni-substituted distorted PFO lattices, while scanning electron microscopy and energy-dispersive spectroscopy indicated a uniform elemental distribution and surface morphology. Polarization vs. electrical field (P−E) measurements showed improved remnant polarization (P_r) with increasing Ni content and synthesis temperatures, achieving a maximum P_r of 66.7 $\mu C/cm^2$ at 5 wt.% The Ni loading and substrate ($Pt/Ti/SiO_2/Si$, Nanoshel Company, Cheshire, UK) temperature were 600 °C. These findings suggest that optimizing the synthesis parameters such as temperature and substitution content is crucial for controlling the ferroelectric properties of PFO thin films.

Keywords: multiferroic; ferroelectrics; $Pb_2Fe_2O_5$; nickel-substituted; reactive magnetron sputtering

Academic Editors: Torsten Brezesinski and Angela De Bonis

Received: 12 December 2024
Revised: 14 January 2025
Accepted: 20 January 2025
Published: 26 January 2025

Citation: Beklešovas, B.; Stankus, V.; Iljinas, A.; Balčiūnaitė, U. Enhancement of Ferroelectric Properties of Ni-Substituted $Pb_2Fe_2O_5$ Thin Films Synthesized by Reactive Magnetron Sputtering Deposition. *Coatings* **2025**, *15*, 143. https://doi.org/10.3390/coatings15020143

1. Introduction

Materials that exhibit the interaction of several basic ferroic features, including ferroelectricity, ferromagnetism, and ferroelasticity, are known as multiferroic materials [1–4]. Developing a variety of applications for non-volatile memory devices, transducers, magnetic field sensors, etc., is made possible by the ability to regulate both ferroelectric and magnetic properties in the same phase [5–10]. Particular focus is given to solid-state memories, which have low power consumption and great storage density due to the ability of multiferroics to write and read data electrically and magnetically. Two processes take place at the same time: magnetism requires transition metal ions with partially filled d orbitals, whereas ferroelectricity results from transition ions with empty d orbitals.

Significant strides have been made in the discovery and development of multiferroics over the last 20 years. There are a lot of materials with coexisting ferroelectric and magnetic order phenomena. One of the most important classes are manganites $YMnO_3$ [11–14], $TbMn_2O_5$ [15,16], $SrMnO_3$ [17], $HoMnO_3$ [18], and $BiMnO_3$ [19] and ferrites $BiFeO_3$ (BFO) [20], $CoFe_2O_4$ [21], $LuFe_2O_4$ [22], etc. Despite the fact that the most studied multiferroic is $BiFeO_3$ (BFO) [20], frequent modification with various substitutions

or combinations with others in composites has not yet led to the required multiferroic properties for the practical application of these materials in high-density memory devices. Lead ferrite $Pb_2Fe_2O_5$ (PFO) is one of the promising ferrite materials, showing simultaneous ferroelectric and magnetic characteristics at room temperature [23–25]. This material's polarization originated from the FeO_6 octahedra in the perovskite-based structure of $Pb_2Fe_2O_5$ as well as the off-centers of displaced Pb^{2+} ions [25]. While the B site produces magnetism, the non-centrosymmetric structures, which are impacted by the existence of $6s^2$ lone pairs and covalent Pb-O bonds, contribute to ferroelectricity (Fe^{3+}) [15].

High leakage current and low magnetoelectric coupling coefficients are two major issues that must be resolved. This issue could be resolved by substituting Pb or Fe with different metal atoms. It is recognized that such changing of the characteristics of multiferroics is a successful strategy. Pb^{2+} (A-site) and Fe^{3+} (B-site) ion substitution can change the characteristics of PFO, just like with BFO. The radius of the Fe^{3+} (0.64 Å) ion is comparable to that of Cr^{3+} (0.76 Å) [26,27], Ti^{4+} (0.68 Å) [28,29], and Mn^{3+} (0.72 Å) [30–32] ions, which might take the place of the Fe^{3+} ion at the B-site.

But when using aliovalent elements, it is important to think about the charge compensation of altered cations. As a result, ions like Cr^{3+}, Ni^{2+}, Co^{2+}, or Nb^5 might be used to preserve charge neutrality and potentially prevent oxygen vacancies [33–36]. The cation–oxygen octahedral configuration may be distorted in this case due to the random occupancy of the B-site by both Fe^{3+} and other element ions. Different super exchange interactions between the Fe-O polyhedra at the corners and adjacent units along the shared edges of the Fe–O_5 tetrahedral pyramids are caused by this arrangement. In our previous work, we demonstrated the successful substitution of Fe^{3+} ions with Cr [37] and Co [38] ions and the enhancing of multiferroic properties in PFO thin films.

This work's aim was to synthesize nickel-substituted lead ferrite thin films and examine how the deposition temperature and concentration of nickel affected the thin films' ferroelectric characteristics, crystal structure, and surface morphology.

Nickel-substituted lead ferrite ($Pb_2Fe_2O_5$) thin films are presented in this work as a unique method to improve the ferroelectric characteristics of multiferroics at room temperature. The results give fresh information about substitution techniques that can greatly enhance the ferroelectric characteristics, which is essential for real-world uses.

2. Materials and Methods

Lead ferrite ($Pb_2Fe_2O_5$) substituted with Ni thin films were synthesized using the developed layer-by-layer direct current reactive magnetron sputtering technique (pacituoti). A platinized silicon Pt/Ti/SiO2/Si (200 nm, 20 nm, 1 μm, and 380 μm thickness; Nanoshel Company, Cheshire, UK) multilayer system was used as a substrate. Platinized substrates are widely used for ferroelectric thin film deposition. Its usefulness relies on several factors, such as platinum's chemical inertness, its closeness to major ferroelectric film temperature expansion coefficients and crystal lattice sizes. As stated above, the thickness of each layer in this system is based on the best platinum surface (least roughness) formation. It was determined [39] that the Ti adhesion layer (which is necessary) of 20 nm least influenced the platinum surface roughness. On the other hand, the aim is to make the platinum electrode as thin as possible, but the roughness is the lowest at a thickness of at least 200 nm. The silicon oxide layer (1 μm of oxidated silicon wafer) is used as barrier layer for preventing interdiffusion between the silicon and upper material phase. Finally, platinum serves as a highly beneficial bottom electrode material for a planar capacitor in this context. High-purity targets (Kurt J. Lesker Company, Dresden, Germany, 3 inches in diameter, with a disc shape and purity of 99.9%) for single elements (Pb, Fe, and Ni) were used for each magnetron. The starting pressure was $5{\cdot}10^{-3}$ Pa. The target-to-substrate

distance was set at 60 mm. For the improvement of adhesion of PFO on platinum, the seeding layer [40–42] of titanium was deposited via magnetron sputtering at 1.3 Pa working pressure in a pure argon environment. The temperature at which this layer was deposited was 750 °C, achieving a thickness of 5 nm. Following the seeding layer deposition, the temperature of the substrate was lowered to the chosen deposition temperature (500 °C, 550 °C, and 600 °C), and the process gas was switched to oxygen while maintaining a working pressure of 1.3 Pa. The PFO films were then formed with deposition carried out in situ for a 1 h period. The amount of nickel was regulated using a controlled-width aperture above the Ni target. After the PFO thin film formation, the aluminum top electrodes were deposited using the thermal evaporation method, thus making a capacitor for the analysis of ferroelectric properties.

The Ni concentration was controlled by determining the deposition rate of Ni oxide (which in our case was identified as Ni_2O_3), measuring the thickness and calculating using the volume and the density, the mass. Using the following chemical Equation (1), which appears on the surface, x (wt.%) was determined.

$$2PbO + (1-x)Fe_2O_3 + xNi_2O_3 \xrightarrow{t = 500\ ^\circ\text{C}-600\ ^\circ\text{C}} Pb_2Fe_{2(1-x)}Ni_{2x}O_5 \quad (1)$$

Thin films of $Pb_2Fe_{2(1-x)}Ni_{2x}O_5$ (where x corresponds to Ni_2O_3 content of 3 wt.%, 5 wt.%, and 10 wt.%) were prepared, referred to as PFONi3, PFONi5, and PFONi10, respectively.

In order to examine the PFO films' structural characteristics, X-ray diffraction (XRD) with a Bruker D8 diffractometer (Bruker, Bruker, Billerica, MA, USA), with monochromatic CuKα radiation in Bragg–Brentano geometry was used. Ferroelectric hysteresis loops were measured using the Sawyer–Tower method [43] with a circuit incorporting a 1 kΩ resistor and a 150 nF reference capacitor at a frequency of 50 Hz and at an ambient temperature of 25 °C. The surface morphology of the films was examined using a scanning electron microscope (S-3400N, Hitachi, Tokyo, Japan) at an operating voltage of 10 kV. Elemental distribution of Fe, Pb, Ni, and O in the films was analyzed via energy-dispersive spectroscopy using a Bruker Quad 5040 spectrometer (AXS Microanalysis GmbH, Hamburg, Germany).

3. Results

Thin films of Ni–Ni-substituted PFO were deposited using heated substrates starting at 550 °C. Figure 1 displays the XRD patterns of pure and substituted nickel lead ferrite thin films. The $Pb_2Fe_2O_5$ peaks can be observed at 31.5°, 38.2°, 43.0°, and 46.5° in the 2θ of the unsubstituted PFO. These diffraction peaks correspond to the (220), (312), (400), and (424) crystallographic planes, respectively (JCPDS-ICDD File No 33-0756) [23,25]. In PFONi3 and PFONi5 thin films only the (312) and (424) planes of the $Pb_2Fe_2O_5$ phase are present, and a low-intensity (220) phase peak is observable in the PFONi10 XRD pattern. In Figure 1, the inset shows a slight shift of the PFO phase (312) peaks in the direction of greater 2θ angles. This shift appears due to the disparity between the ionic radii of Ni^{2+} (0.69 Å) and Fe^{3+} (0.64 Å), where substitution between these ions results in a small lattice distortion. The variations in the structure can be an indication of the coexistence of pure and Ni-substituted PFO lattices [44,45]. The crystallite size, calculated using the Scherrer equation was 34 nm (PFONi3), 36 nm (PFONi5), and 37 nm (PFONi10).

The reduction in the intensity of the primary $Pb_2Fe_2O_5$ peaks in the XRD patterns of Ni-substituted PFO thin films can be attributed to several factors. Since their ionic radii are similar, yet slightly different, nickel ions take the place of iron ions when they are integrated into the PFO lattice. This substitution induces lattice distortions, as Ni^{2+} ions are larger than Fe^{3+} ions, disrupting the regular crystal structure and resulting in reduced crystallinity. Due to these distortions, the diffraction peak intensities may be affected. Additionally,

variations in the preferred orientation of the crystals might occur due to the presence of Ni, leading to altered crystal growth and orientation. Owing to these factors, some peaks diminish or disappear entirely, while others become more prominent (Figure 1).

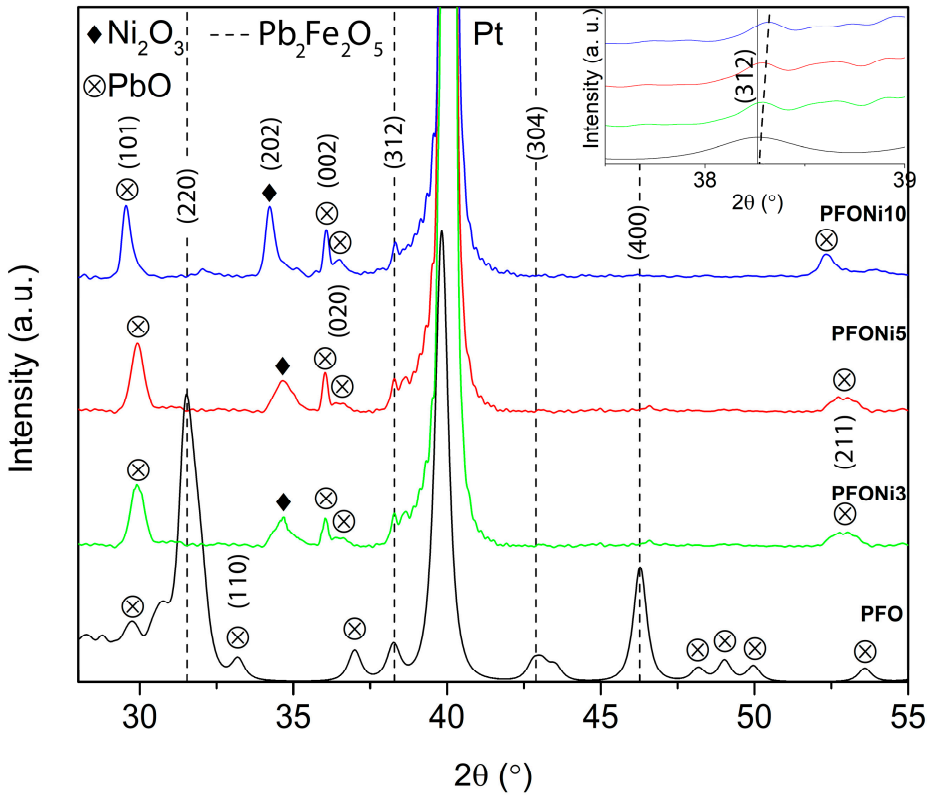

Figure 1. The XRD pattern of the Ni-substituted PFO thin films synthesized at 550 °C.

To evaluate the effect of synthesis temperature, the PFONi5 sample was chosen. We selected the PFONi5 sample to evaluate the temperature influence on the properties because it represents an intermediate nickel content level, providing a balance between the low content in PFONi3 and the higher content in PFONi10. This choice allows us to investigate how temperature affects a sample with moderate nickel substitution, where potential property enhancements due to substitution are neither minimal nor extreme. The deposition of thin films was performed at 500 °C, 550 °C, and 600 °C. It should be mentioned that no PFO phases were observed below 500 °C (for example, at 450 °C). Figure 2 displays the XRD spectra for these films at temperatures between 500 and 600 °C. At 2θ angles of 32.5°, 38.2°, and 46.5°, peaks representing the PFO phases (220), (312), and (400) were detected. For samples synthesized at 500 °C and 600 °C the (220) PFO peak is observed, but its intensity diminished when the temperature of deposition reached 600 °C (Figure 2). The (312) peak became more pronounced and broadened with rising temperature, likely due to lead desorption and evaporation disrupting the stoichiometry. Crystallite size, calculated by the Scherrer equation was 27 nm (500 °C), 36 nm (550 °C), and 51 nm (600 °C).

The presence of a Ni_2O_3 phase was identified at 34.5° in the XRD pattern (JCPDS Card Number 014-01481). As the synthesis temperature increased to 550 °C, the intensity of this phase decreased, suggesting a more effective substitution of Fe^{3+} ions with Ni^{2+} ions at higher temperatures. Peaks representing the PbO phases were found at 30°, 36°, 37°, and 54° 2θ (JCPDS Card Number 76-1796). A clearly visible peak appeared at 54 only in the film synthesized between 500 °C and 550 °C [46]. While the intensities of these PbO peaks fluctuated with temperature, their positions remained consistent. This intensity variation is

a result of altered film stoichiometry caused by a higher temperature, which enhanced lead evaporation and desorption. The angle and intensity of the PFO phase remained consistent when the deposition temperature was raised from 500 °C to 600 °C, except for the PFO (220) phase peak, which significantly reduced in the sample synthesized at 600 °C. Changes in coating stoichiometry are the cause of this peak-intensity movement [47].

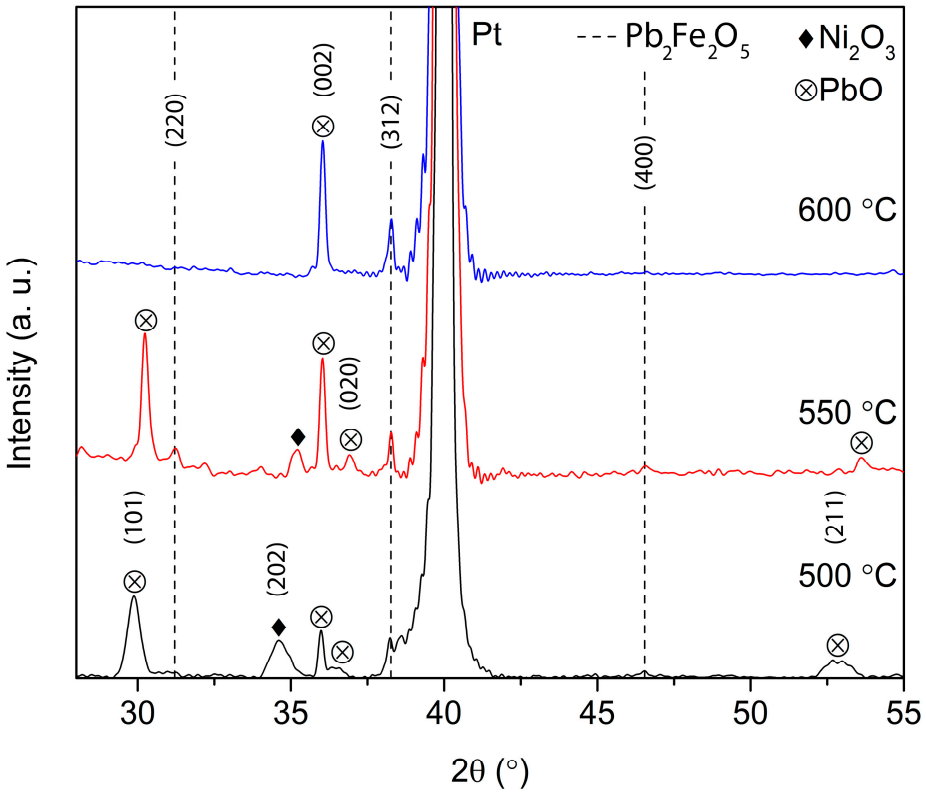

Figure 2. XRD spectra of PFONi5 films deposited at different temperatures.

The study focused on achieving a pure PFO crystallographic phase with changes in lattice distortion, using changes in Ni substitution concentration and synthesis temperature. However, this goal has not yet been realized, because remnant phases of single oxides (PbO and Ni_2O_3) were observed. Abakumov et al. [48] and Wang et al. [25] determined in their research the chemical composition of lead ferrite that can be expressed as $PbFeO_{2.5-x}PbO$ (where x = 0.0625, 0.1, or 0.125), a result of crystallographic shear planes and defect formation during synthesis. This generalized formula indicates the complexity of forming pure PFO phases and avoiding secondary lead oxide phases. This research focused on understanding what specific factors affect the PFO phase formation and revealed that avoiding the presence of residual phases remains a challenge. Adjustments to the synthesis parameters, such as reducing the deposition rate, applying a bias voltage, or using an argon–oxygen mixture instead of pure oxygen, may be necessary [49,50].

The Ni-substituted PFO thin film's surface morphological characteristics were investigated using SEM images. Figure 3 presents images of Ni-substituted PFO thin films synthesized at different temperatures (within the range of 500 °C to 600 °C) and with varying Ni content. In Figure 3a–c, surface images are presented, the distinct structures with well-defined intercrystalline boundaries (except for the sample synthesized at 600 °C) are observed. Relatively prominent boundaries between grains are visible in the film deposited at 550 °C. The density of the grains rises with the synthesis temperature, producing a remarkably homogeneous and dense surface at 600 °C. In Figure 3b, it is observed that the structures start to form clusters, leading to an expansion along the short axis of the grain.

As seen in Figure 3c, for the PFO films synthesized at 600 °C, it was difficult to measure the size of individual grains due to the formation of very dense structures.

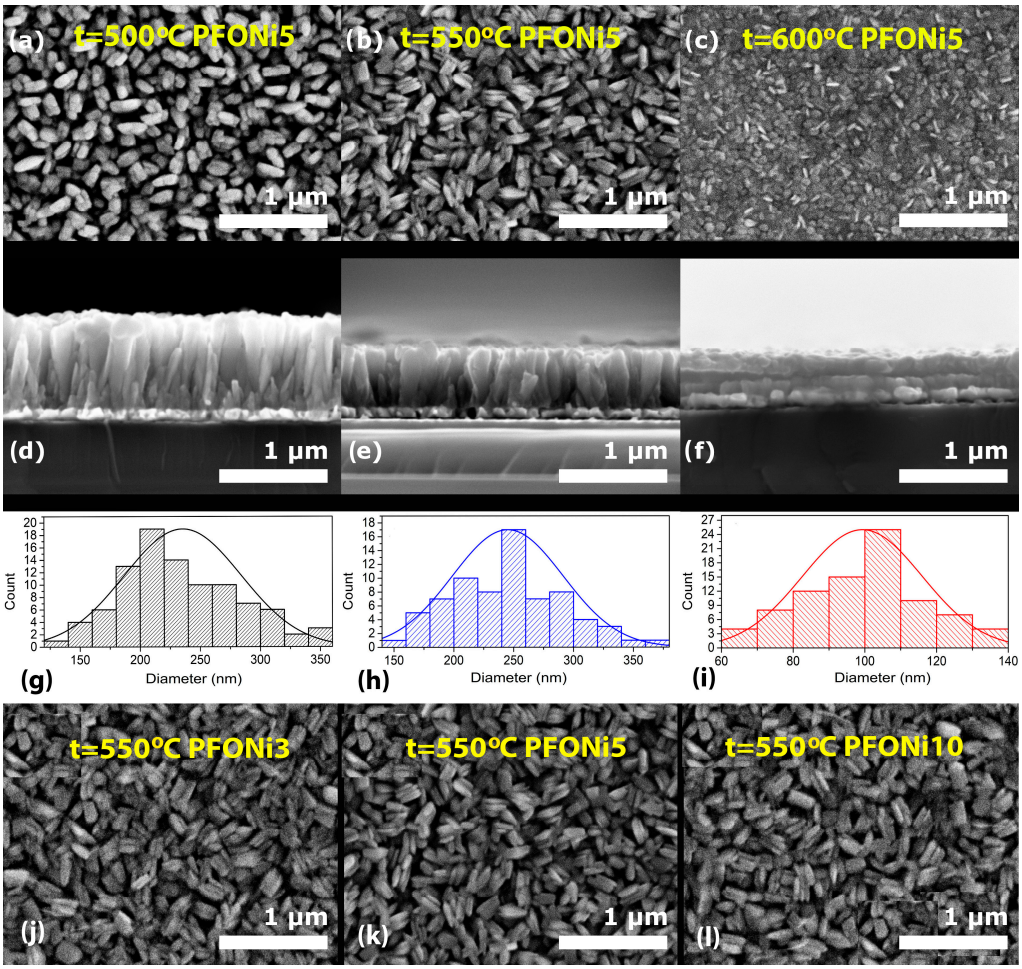

Figure 3. Surface and cross-sectional SEM views of PFONi5 films formed at (**a**,**d**) 500 °C, (**b**,**e**) 550 °C, and (**c**,**f**) 600 °C with grain size distribution shown in (**g**–**i**). Surface views of PFONi3 (**j**), PFONi5 (**k**), and PFONi10 (**l**) films formed at 550 °C.

The cross-sectional view of the thin films is presented in Figure 3d–f. These images reveal columnar growth during film formation. When comparing the samples made at 500 °C and 550 °C (Figure 3d and e, respectively), it is clear that the columns get wider as the synthesis temperature rises. At a synthesis temperature of 600 °C (Figure 3f), dense structures are observed, making it difficult to determine the dimensions of the separate columns. The dependence of structure density on temperature can be explained similarly to the case of Cr-substituted PFO [37]; at high synthesis temperatures, atoms gain more energy and can diffuse further along the surface to the growth centers, resulting in dense structures. The variation in film thickness can also be attributed to this increased atomic mobility, which influences density. The thin film synthesized at 600 °C reaches 410 nm in thickness, whereas samples deposited at 550 °C and 500 °C, with less dense grain structures, exhibit thicknesses of 550 nm and 840 nm, respectively. Another factor contributing to thinner films at higher synthesis temperatures is lead evaporation. Because of its relatively low melting point, (~327 °C), higher synthesis temperatures, such as 600 °C, give lead atoms more kinetic energy, which causes them to evaporate and desorb from the film's surface during the growing process [51,52]. The result of that is a decrease in the lead deposition rate and thickness in general. The grain size distributions are shown in Figure 3g–i for the thin films deposited at 500 °C, 550 °C, and 600 °C, indicating average grain sizes of

approximately 245 nm, 235 nm, and 99 nm, respectively. The SEM images in Figure 3j–l of PFONi3, PFONi5, and PFONi10 samples synthesized at 550 °C exhibit similar surface morphologies, with no significant variations in grain structure across the different Ni concentrations. The uniformity in grain size and distribution suggests that the Ni doping levels do not substantially influence the grain structure, indicating that the crystallization process remains consistent regardless of the Ni content.

Figure 4 displays the elemental distribution in a PFONi5 film that was formed at 550 °C. It is observed that iron and lead are densely and uniformly distributed across the sample's surface, with no observable artifacts. Nickel is uniformly distributed across the surface as well; however, because of its lower concentration, it occurs less frequently than iron and lead. The even dispersion of elements, as indicated by EDS mapping, demonstrates that lead, nickel, and oxygen are homogeneously distributed throughout the film. The nickel content was measured at 4.9 ± 0.4 wt.%, and oxygen accounted for 17.8 ± 1.3 wt.%. The iron and lead concentrations were determined to be 48.1 ± 1.2 wt.% and 29.1 ± 0.4 wt.%, respectively. The phases identified with XRD, such as Ni_2O_3 and PbO, are present in an evenly dispersed or nanocrystalline state, which is observed in the EDS mapping.

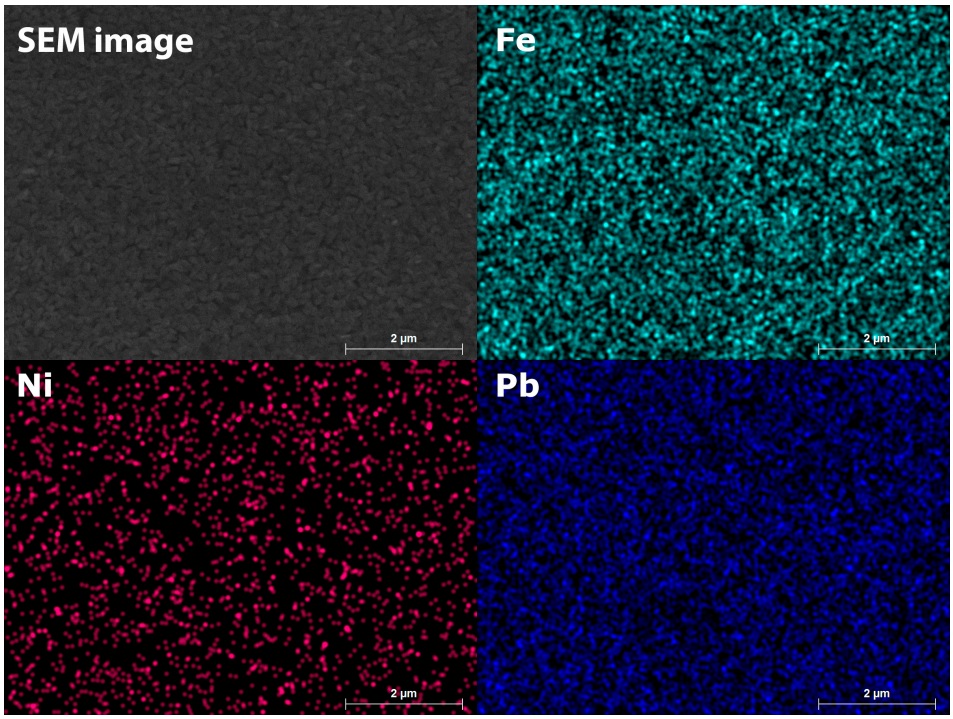

Figure 4. Views of the EDX mapping of the PFONi5 film synthesized at 550 °C.

As illustrated in Figure 5, ferroelectric (P-E) hysteresis loops were tested at room temperature to examine the impact of the substitution concentration and deposition temperature on the ferroelectric properties of PFO. It can be observed that the nickel-substituted ferroelectric characteristics of $Pb_2Fe_2O_5$ thin films demonstrate a dependence on the substitution concentration and deposition temperature. Figure 5a shows how the nickel content impacts the ferroelectric properties of PFO thin films that were synthesized at 550 °C. The remnant polarization in the PFONi10 thin film is 63.2 $\mu C/cm^2$, which is significantly higher than in the lower Ni content PFONi3 sample with P_r of 53.3 $\mu C/cm^2$.

The reason for this enhancement is that substituting Fe^{3+} ions with larger Ni^{2+} ions within the Fe-O octahedron induces lattice distortions and a larger non-centrosymmetry, leading to increased ferroelectric polarization in general [53,54]. It should be mentioned, that increasing the concentration over 10% (by wt.%) did not make changes to the remnant

polarization value. Higher substitution concentrations can introduce structural disorder, disrupting the long-range ferroelectric order and leading to saturated remnant polarization [55,56]. Although the remnant polarization values increased with an increase in the Ni content, the P-E loops exhibit a rounded shape indicating the unsaturated sample nature. This could be the result of the leakage currents in the films. The placing of Ni^{2+} in proximity to the Fe^{3+} ions is compensated for by the substituted lower valence Ni^{2+}, resulting in the generation of vacancies of oxygen, which results in an increased density of unbound charges. Oxygen vacancies act as the pinning centers, thus preventing polarization switching, resulting in increased coercive field values [54,57].

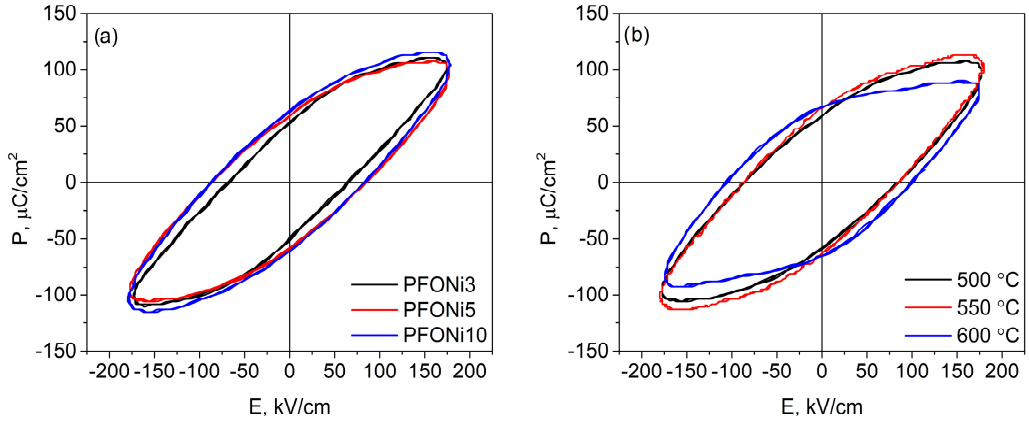

Figure 5. Comparison of P−E curves showing the nickel concentration influence on substituted PFO, deposited at 550 °C (**a**), and the synthesis temperature influence on PFONi5 samples (**b**).

Figure 5b shows how the ferroelectric characteristics of PFONi5 samples are affected by the synthesis temperature, which is between 500 and 600 °C. When PFONi5 is synthesized at 500 °C, its coercive field (E_c) is 85.7 kV/m and its remnant polarization (P_r) is 58.7 μC/cm^2. The coercive field stays almost constant at 85.6 kV/m, while the remnant polarization of PFONi5 increases by around 12% when the temperature is raised to 550 °C. At the maximum temperature of 600 °C of synthesis, the dielectric properties reach the upper limit, with P_r reaching 66.7 μC/cm^2 and E_c increasing to 102.9 kV/m. The P-E hysteresis exhibits a similar oval shape as in the samples represented in Figure 5a, which may indicate the same reasons for such behavior. The samples deposited at temperatures above 600 °C did not exhibit ferroelectric hysteresis.

Figure 6 represents the ferroelectric properties' dependence on the synthesis properties—substitution concentration and synthesis temperature. The impact of Ni concentration on the PFO structure is seen in Figure 6a. Remnant polarization and coercive field values were found to rise with Ni concentration; for the PFONi3 sample, they start at a P_r of 53.3 μC/cm^2 and E_c of 64 kV/m, and for the PFONi10 sample, they reach a P_r of 63.2 μC/cm^2 and an E_c of 86 kV/m. Such a trend can be explained as the Ni^{2+} ion substituting for Fe^{3+}. This causes the Fe-O octahedron to have a larger ion off-center. Although a positive change in remnant polarization is observed, the increase in remnant polarization diminishes at higher Ni content. This can be attributed to an increased defect concentration, which disrupts the long-range ferroelectric order [55,56].

Figure 6b displays the ferroelectric properties of the PFONi5 samples' dependence on the synthesis temperature within a range of 500 °C to 600 °C. The thin film synthesized at the lowest temperature of 500 °C exhibits a P_r of 58.7 μC/cm^2 and an E_c of 85.7 kV/m, respectively. The ferroelectric properties increase with the synthesis temperature; additionally, the P_r and E_c values reach 66.7 μC/cm^2 and 102.9 kV/m, respectively, at 600 °C. These ferroelectric properties can be attributed to structural film properties. From the results

in Table 1 and Figure 6b, we see clearly that the structure of the thin films impacts the ferroelectric properties drastically. It can be explained by the grain size effect and compactification (density) of the material. As we saw when the grains were larger, the density of the structure is smaller and vice versa (Figure 3a–f). Physically, the size of ferroelectric domains can be limited by grain size, but in dense structures, grains are merging, which leads to the merging of domains, thereby increasing the general polarization.

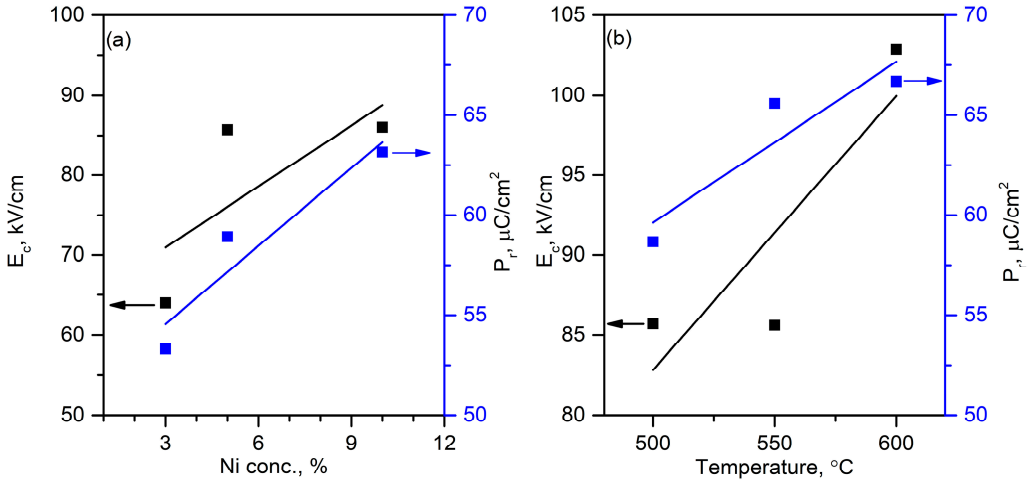

Figure 6. Effects of varying nickel concentrations on the ferroelectric characteristics of PFO films synthesized at 550 °C (**a**), and PFONi5 film ferroelectric properties (**b**) as a function of synthesis temperature.

Table 1. Comparative characteristics of Ni-substituted and pure PFO thin films.

Sample	t, °C	Thickness, nm	Grain Size, nm	Crystallite Size, nm	Ni Concentration			P_r, μC/cm^2	E_c, kV/m
					$x(Ni_2O_3)$, wt.%	by Mass *n*, at%	by EDS *n*, at%		
PFONi5	500	840	245	27	5	10	9.3	58.7	85.7
PFONi5	550	550	235	36	5	10	9.3	60.1	85.6
PFONI5	600	410	99	51	5	10	9.3	66.7	102.9
PFONi3	550	550	235	34	3	6	4.8	53.3	64
PFONi10	550	550	235	37	10	20	21.2	63.2	86
PFO [23]	550	550	243	16	0	0	0	49.6	42.9

The density of grain boundaries and other defects, such as oxygen vacancies, which act as pinning centers and affect polarization, can be minimized at elevated synthesis temperatures. Furthermore, the higher synthesis temperatures can improve ion mobility resulting in better distribution and ordering of substitution ions [54].

To summarize the investigation of the ferroelectric properties of Ni-substituted PFO thin films, it should be noted that these properties can be controlled by varying both the substitution concentration and the synthesis temperature (Table 1).

4. Conclusions

The study demonstrated that Ni-substituted $Pb_2Fe_2O_5$ (PFO) thin films exhibit notable changes in structural, morphological, and ferroelectric properties depending on the added Ni concentration and synthesis temperature. Thin films of $PbFeO_5$ substituted with Ni are composed of $Pb_2Fe_2O_5$ and PbO phases, along with a minor presence of Ni_2O_3 phases. Higher synthesis temperatures primarily influenced the formation of PbO phases. Increasing the synthesis temperature resulted in denser grain structures and reduced film thickness, attributed to lead evaporation. Surface analysis revealed a uniform distribution

of Ni, Pb, Fe, and O. Ferroelectric property analysis showed that higher Ni concentrations and synthesis temperatures enhanced the remnant polarization and coercive field. The highest values of remnant polarization (66.7 $\mu C/cm^2$) and coercive field (102.9 kV/m) were observed at 600 °C with 5 wt.% Ni substitution. P-E hysteresis curves also indicated leakage currents caused by oxygen vacancies. The findings suggest that optimizing synthesis parameters such as temperature and substitution content is crucial for controlling the ferroelectric properties of PFO thin films.

Author Contributions: Conceptualization, B.B. and V.S.; methodology, A.I.; validation, V.S., A.I. and B.B.; investigation, B.B. and V.S.; writing—original draft preparation, U.B. and B.B.; writing—review and editing, B.B. and V.S.; visualization, U.B.; All authors have read and agreed to the published version of the manuscript.

Funding: This research received no external funding.

Institutional Review Board Statement: Not applicable.

Informed Consent Statement: Not applicable.

Data Availability Statement: The original contributions presented in the study are included in the article; further inquiries can be directed to the corresponding author.

Conflicts of Interest: The authors declare no conflicts of interest.

References

1. Huang, W.; Yang, S.; Li, X. Multiferroic heterostructures and tunneling junctions. *J. Mater.* **2015**, *1*, 263–284. [CrossRef]
2. Khomskii, D.I. Multiferroics: Different ways to combine magnetism and ferroelectricity. *J. Magn. Magn. Mater.* **2006**, *306*, 1–8. [CrossRef]
3. Roy, S.; Majumder, S.B. Recent advances in multiferroic thin films and composites. *J. Alloys Compd.* **2012**, *538*, 153–159. [CrossRef]
4. Sekine, Y.; Akiyoshi, R.; Hayami, S. Recent advances in ferroelectric metal complexes. *Coord. Chem. Rev.* **2022**, *469*, 214663. [CrossRef]
5. Amirov, A. Chapter 15—Multiferroic, magnetic, and magnetoelectric nanomaterials for medical applications. In *Magnetic Materials and Technologies for Medical Applications*; Tishin, A.M., Ed.; Woodhead Publishing: Sawston, UK, 2022; pp. 469–484.
6. Pati, D.K.; Das, P.R.; Parida, B.N.; Padhee, R. Multifunctional characterization of multiferroic $[Pb(Fe_{0.5}Nb_{0.5})O_3]_{0.5}$—$[(Ca_{0.2}Sr_{0.8})TiO_3]_{0.5}$ for storage and photocatalytic applications. *Ceram. Int.* **2022**, *48*, 19344–19357. [CrossRef]
7. Rahul, M.T.; Chacko, S.K.; Vinodan, K.; Raneesh, B.; Philip, K.A.; Bhadrapriya, B.C.; Bose, B.A.; Kalarikkal, N.; Rouxel, D.; Viswanathan, P.; et al. Multiferroic and energy harvesting characteristics of P(VDF-TrFE)-$CuFe_2O_4$ flexible films. *Polymer* **2022**, *252*, 124910. [CrossRef]
8. Shah, J.; Verma, K.C.; Agarwal, A.; Kotnala, R.K. Novel application of multiferroic compound for green electricity generation fabricated as hydroelectric cell. *Mater. Chem. Phys.* **2020**, *239*, 122068. [CrossRef]
9. Singh Pawar, M.; Raj, A.; Kumar Singh, A.; Tuli, V.; Anshul, A.; Kumar, M. Lead-free 'Ca' doped $Bi_{0.80}La_{0.20}FeO_3$ multiferroic material for solar cell applications. *Mater. Today Proc.* **2022**, *67*, 713–718. [CrossRef]
10. Vopson, M.M. Fundamentals of Multiferroic Materials and Their Possible Applications. *Crit. Rev. Solid State Mater. Sci.* **2015**, *40*, 223–250. [CrossRef]
11. Van Aken, B.B.; Palstra, T.T.M.; Filippetti, A.; Spaldin, N.A. The origin of ferroelectricity in magnetoelectric $YMnO_3$. *Nat. Mater.* **2004**, *3*, 164–170. [CrossRef] [PubMed]
12. Watanabe, K.; Nishikawa, M.; Sakaguchi, H.; Veis, M.; Ishibashi, T. Preparation and characterization of $YMnO_3$ thin films by metal–organic decomposition. *Jpn. J. Appl. Phys.* **2023**, *62*, SB1005. [CrossRef]
13. López-Alvarez, M.Á.; Silva-Jara, J.M.; Silva-Galindo, J.G.; Reyes-Becerril, M.; Velázquez-Carriles, C.A.; Macías-Rodríguez, M.E.; Macías-Lamas, A.M.; García-Ramírez, M.A.; López de Alba, C.A.; Reynoso-García, C.A. Determining the Photoelectrical Behavior and Photocatalytic Activity of an h-$YMnO_3$ New Type of Obelisk-like Perovskite in the Degradation of Malachite Green Dye. *Molecules* **2023**, *28*, 3932. [CrossRef] [PubMed]
14. Zhang, Q.; Tan, G.; Gu, L.; Yao, Y.; Jin, C.; Wang, Y.; Duan, X.; Yu, R. Direct Observation of Multiferroic Vortex Domains in $YMnO_3$. *Sci. Rep.* **2013**, *3*, 2741. [CrossRef] [PubMed]
15. Endichi, A.; Bouhani, H.; Zaari, H.; Balli, M.; Mounkachi, O.; El Kenz, A.; Benyoussef, A.; Mangin, S. Electronic and magnetic properties of the multiferroic $TbMn_2O_5$. *Appl. Phys. A* **2020**, *126*, 410. [CrossRef]
16. Tolédano, P.; Schranz, W.; Krexner, G. Induced ferroelectric phases in $TbMn_2O_5$. *Phys. Rev. B* **2009**, *79*, 144103. [CrossRef]

17. Ricca, C.; Berkowitz, D.; Aschauer, U. Ferroelectricity promoted by cation/anion divacancies in $SrMnO_3$. *J. Mater. Chem. C* **2021**, *9*, 13321–13330. [CrossRef] [PubMed]
18. Windsor, Y.W.; Ramakrishnan, M.; Rettig, L.; Alberca, A.; Lippert, T.; Schneider, C.W.; Staub, U. Multiple magnetic ordering phenomena in multiferroic o-$HoMnO_3$. *Phys. Rev. B* **2020**, *102*, 214423. [CrossRef]
19. Hanif, S.; Hassan, M.; Riaz, S.; Atiq, S.; Hussain, S.S.; Naseem, S.; Murtaza, G. Structural, magnetic, dielectric and bonding properties of $BiMnO_3$ grown by co-precipitation technique. *Results Phys.* **2017**, *7*, 3190–3195. [CrossRef]
20. Wu, J.; Fan, Z.; Xiao, D.; Zhu, J.; Wang, J. Multiferroic bismuth ferrite-based materials for multifunctional applications: Ceramic bulks, thin films and nanostructures. *Prog. Mater. Sci.* **2016**, *84*, 335–402. [CrossRef]
21. Dedi; Idayanti, N.; Kristiantoro, T.; Alam, G.F.N.; Sudrajat, N. Magnetic properties of cobalt ferrite synthesized by mechanical alloying. *AIP Conf. Proc.* **2018**, *1964*, 020003. [CrossRef]
22. Kim, Y.J.; Konishi, S.; Hayasaka, Y.; Kakeya, I.; Tanaka, K. Magnetic and electrical properties of $LuFe_2O_4$ epitaxial thin films with a self-assembled interface structure. *CrystEngComm* **2020**, *22*, 1096–1105. [CrossRef]
23. Beklešovas, B.; Stankus, V.; Link, J.; Stern, R. Structural, ferroelectric and magnetic properties of lead ferrite ($Pb_2Fe_2O_5$) thin films synthesized by reactive magnetron deposition. *Thin Solid Film.* **2020**, *708*, 138124. [CrossRef]
24. Hadermann, J.; Abakumov, A.M.; Nikolaev, I.V.; Antipov, E.V.; Van Tendeloo, G. Local structure of perovskite-based "$Pb_2Fe_2O_5$". *Solid State Sci.* **2008**, *10*, 382–389. [CrossRef]
25. Wang, M.; Tan, G. Multiferroic properties of $Pb_2Fe_2O_5$ ceramics. *Mater. Res. Bull.* **2011**, *46*, 438–441. [CrossRef]
26. Sinha, A.K.; Bhushan, B.; Jagannath; Sharma, R.K.; Sen, S.; Mandal, B.P.; Meena, S.S.; Bhatt, P.; Prajapat, C.L.; Priyam, A.; et al. Enhanced dielectric, magnetic and optical properties of Cr-doped $BiFeO_3$ multiferroic nanoparticles synthesized by sol-gel route. *Results Phys.* **2019**, *13*, 102299. [CrossRef]
27. Kim, J.K.; Kim, S.S.; Kim, W.J.; Bhalla, A.S.; Guo, R. Enhanced ferroelectric properties of Cr-doped $BiFeO_3$ thin films grown by chemical solution deposition. *Appl. Phys. Lett.* **2006**, *88*, 132901. [CrossRef]
28. Wang, Y.; Nan, C.W. Site modification in BiFeO3 thin films studied by Raman spectroscopy and piezoelectric force microscopy. *J. Appl. Phys.* **2008**, *103*, 114104. [CrossRef]
29. Liu, H.; Liu, Z.; Yao, K. Improved electric properties in $BiFeO_3$ films by the doping of Ti. *J. Sol-Gel Sci. Technol.* **2007**, *41*, 123–128. [CrossRef]
30. Singh, S.K.; Ishiwara, H.; Maruyama, K. Room temperature ferroelectric properties of Mn-substituted $BiFeO_3$ thin films deposited on Pt electrodes using chemical solution deposition. *Appl. Phys. Lett.* **2006**, *88*, 262908. [CrossRef]
31. Singh, S.K.; Menou, N.; Funakubo, H.; Maruyama, K.; Ishiwara, H. (111)-textured Mn-substituted $BiFeO_3$ thin films on $SrRuO_3/Pt/Ti/SiO_2/Si$ structures. *Appl. Phys. Lett.* **2007**, *90*, 242914. [CrossRef]
32. Wen, Z.; Hu, G.; Fan, S.; Yang, C.; Wu, W.; Zhou, Y.; Chen, X.; Cui, S. Effects of annealing process and Mn substitution on structure and ferroelectric properties of $BiFeO_3$ films. *Thin Solid Film.* **2009**, *517*, 4497–4501. [CrossRef]
33. Hoque, M.M.; Islam, M.T.; Islam, M.R.; Zubair, M.A. Effective bandgap tuning with non-trivial modulation in room temperature magnetic and electrical responses of low level Ba–Cr co-substituted $BiFeO_3$ nanoparticles. *Ceram. Int.* **2022**, *48*, 19583–19596. [CrossRef]
34. Tefera Kebede, M.; Devi, S.; Dillu, V.; Chauhan, S. Effects of Sm and Cr co-doping on structural, magnetic, optical and photocatalytic properties of $BiFeO_3$ nanoparticles. *Mater. Sci. Eng. B* **2022**, *283*, 115859. [CrossRef]
35. Beklešovas, B.; Iljinas, A.; Stankus, V.; Čyvienė, J.; Andrulevičius, M.; Ivanov, M.; Banys, J. Structural, Morphologic, and Ferroelectric Properties of PZT Films Deposited through Layer-by-Layer Reactive DC Magnetron Sputtering. *Coatings* **2022**, *12*, 717. [CrossRef]
36. Iljinas, A.; Stankus, V. Structural and ferroelectric properties of bismuth ferrite thin films deposited by direct current reactive magnetron sputtering. *Thin Solid Film.* **2016**, *601*, 106–110. [CrossRef]
37. Beklešovas, B.; Stankus, V.; Abakevičienė, B.; Link, J.; Stern, R.; Plyushch, A.; Banys, J.; Čyvienė, J.; Girčys, R.; Bašinskas, M.; et al. Synthesis and Characterization of Cr-Doped $Pb_2Fe_2O_5$ Thin Films by Reactive Magnetron Sputtering. *ECS J. Solid State Sci. Technol.* **2023**, *12*, 103014. [CrossRef]
38. Beklešovas, B.; Stankus, V.; Iljinas, A.; Marcinauskas, L. Ferroelectric and Structural Properties of Cobalt-Doped Lead Ferrite Thin Films Formed by Reactive Magnetron Sputtering. *Crystals* **2024**, *14*, 721. [CrossRef]
39. Bernhardt, G.; Silvestre, C.; LeCursi, N.; Moulzolf, S.C.; Frankel, D.J.; Lad, R.J. Performance of Zr and Ti adhesion layers for bonding of platinum metallization to sapphire substrates. *Sens. Actuators B Chem.* **2001**, *77*, 368–374. [CrossRef]
40. Coulibaly, M.D.; Borderon, C.; Renoud, R.; Gundel, H.W. Enhancement of $PbZrO_3$ polarization using a Ti seed layer for energy storage application. *Thin Solid Film.* **2020**, *716*, 138432. [CrossRef]
41. Jun, Y.U.; Gang, P.; Yunbo, W.; Longhai, W.; Jia, L.I.; Junxiong, G.A.O. The effect of seeding layers on ferroelectric properties of PTZT thin films. *Integr. Ferroelectr.* **2006**, *85*, 59–66. [CrossRef]
42. Gong, W.; Li, J.-F.; Chu, X.; Gui, Z.; Li, L. Preparation and characterization of sol–gel derived (100)-textured $Pb(Zr,Ti)O_3$ thin films: PbO seeding role in the formation of preferential orientation. *Acta Mater.* **2004**, *52*, 2787–2793. [CrossRef]

43. Delimova, L.A.; Guschina, E.V.; Yuferev, V.S.; Grekhov, I.V.; Seregin, D.S.; Vorotilov, K.A.; Sigov, A.S. Electrophysical Properties of Integrated Ferroelectric Capacitors Based on Sol-Gel PZT Films. *Ferroelectrics* **2015**, *484*, 32–42. [CrossRef]
44. Kumar, Y.; Mohiddon, M.; Srivastava, A.; Yadav, K.L. Effect of Ni doping on structural and dielectric properties of $BaTiO_3$. *Indian J. Eng. Mater. Sci.* **2009**, *16*, 390.
45. Akhil Raman, T.S.; Nair, V.R.; Raju, K.C.J. Effect of Nickel and Cobalt co-substitution on the structural and dielectric properties of Barium Titanate ceramics. *J. Mater. Sci. Mater. Electron.* **2020**, *31*, 21747–21757. [CrossRef]
46. Gil, D.M.; Nieva, G.; Franco, D.G.; Gómez, M.I.; Carbonio, R.E. Lead nitroprusside: A new precursor for the synthesis of the multiferroic $Pb_2Fe_2O_5$, an anion-deficient perovskite. *Mater. Chem. Phys.* **2013**, *141*, 355–361. [CrossRef]
47. Thongrit, P.; Chananonnawathorn, C.; Horprathum, M.; Triamnak, N.; Lertvanithphol, T.; Eitssayeam, S.; Pengpat, K.; Bintachitt, P. Improving the microstructure and properties of PZT thin films via annealing prepared by RF magnetron sputtering using $Pb(Zr_{0.52}Ti_{0.48})O_3$ target. *Ceram. Int.* **2023**, *49*, 12912–12924. [CrossRef]
48. Abakumov, A.M.; Hadermann, J.; Van Tendeloo, G.; Antipov, E.V. Chemistry and Structure of Anion-Deficient Perovskites with Translational Interfaces. *J. Am. Ceram. Soc.* **2008**, *91*, 1807–1813. [CrossRef]
49. Jeongok, C.; Jeungsun, A.; Lee, K. Multiferroic $BiFeO_3$ Thin Films Prepared by Using a Conventional RF Magnetron Sputtering Method. *J. Korean Phys. Soc.* **2009**, *54*, 844–848. [CrossRef]
50. Qi, X.; Tsai, P.-C.; Chen, Y.-C.; Lin, Q.-R.; Huang, J.-C.-A.; Chang, W.-C.; Chen, I.-G. Optimal growth windows of multiferroic $BiFeO_3$ films and characteristics of ferroelectric domain structures. *Thin Solid Film.* **2009**, *517*, 5862–5866. [CrossRef]
51. Cartwright, J.H.E.; Escribano, B.; Piro, O.; Sainz-Diaz, C.I.; Sánchez, P.A.; Sintes, T. Ice Film Morphologies and the Structure Zone Model. *AIP Conf. Proc.* **2008**, *982*, 696–701. [CrossRef]
52. Kaiser, N. Review of the fundamentals of thin-film growth. *Appl. Opt.* **2002**, *41*, 3053–3060. [CrossRef] [PubMed]
53. Atiq, S.; Fatima, A.; Khalid, M.; Hassan, A.; Mustafa, G.M.; Siddiqi, S.A.; Naseem, S. Multifunctionality of magnetoelectrically coupled Ni/Cr co-doped $BiFeO_3$ multiferroics. *J. Alloys Compd.* **2019**, *789*, 400–408. [CrossRef]
54. Annapu Reddy, V.; Pathak, N.P.; Nath, R. Enhanced magnetoelectric coupling in transition-metal-doped $BiFeO_3$ thin films. *Solid State Commun.* **2013**, *171*, 40–45. [CrossRef]
55. Hao, S.; Yao, M.; Vitali-Derrien, G.; Gemeiner, P.; Otoničar, M.; Ruello, P.; Bouyanfif, H.; Janolin, P.-E.; Dkhil, B.; Paillard, C. Optical absorption by design in a ferroelectric: Co-doping in $BaTiO_3$. *J. Mater. Chem. C* **2022**, *10*, 227–234. [CrossRef]
56. Peng, H.; Wu, T.; Liu, Z.; Fu, Z.; Wang, D.; Hao, Y.; Xu, F.; Wang, G.; Chu, J. High-entropy relaxor ferroelectric ceramics for ultrahigh energy storage. *Nat. Commun.* **2024**, *15*, 5232. [CrossRef] [PubMed]
57. Duong, N.X.; Bae, J.-S.; Jeon, J.; Lim, S.Y.; Oh, S.H.; Ullah, A.; Sheeraz, M.; San Choi, J.; Ko, J.-H.; Yang, S.M.; et al. Polymorphic phase transition in $BaTiO_3$ by Ni doping. *Ceram. Int.* **2019**, *45*, 16305–16310. [CrossRef]